energies

MDPI

Article

A Modified Decentralized Droop Control Method to Eliminate Battery Short-Term Operation in a Hybrid Supercapacitor/Battery Energy Storage System

Pavlos Papageorgiou , Konstantinos Oureilidis , Anna Tsakiri and Georgios Christoforidis *

Department of Electrical and Computer Engineering, University of Western Macedonia, ZEP Campus,
50150 Kozani, Greece; p.papageorgiou@uowm.gr (P.P.); koureilidis@uowm.gr (K.O.); mpa00085@uowm.gr (A.T.)
* Correspondence: gchristoforidis@uowm.gr; Tel.: +30-24610-68141

Abstract: Employment of a battery energy storage system to compensate for the generation-consumption mismatch is a vital element for a resilient microgrid. However, the frequent (i.e., short-term) cyclic activity and the abrupt current variations (i.e., high di/dt) have adverse effects on the energy-type battery's lifespan. On the other hand, the power-type supercapacitor energy storage system (SCES) has almost zero lifetime degradation when it is subjected to irregular charging/discharging patterns. Therefore, the hybridization between them can reduce battery stress levels. This study proposes a droop control algorithm with multiple segments for a SCES/battery hybrid energy storage system (HESS) that is employed in a solar/wind DC microgrid. The presented control scheme is decentralized since it avoids the central controller (CC) and the communication links between the controllers of SCES and battery units. To eliminate the short-term cyclic operation of the battery, the SCES regulates the bus voltage inside a narrow zone with a droop curve that exploits all its available energy capacity. Inside this zone, the battery is kept inactive. As soon as the bus voltage deviates from this band, the SCES enters the idle mode, and the battery is triggered following a droop curve different for charging or discharging mode to stabilize the bus voltage. To evaluate the effectiveness of the proposed system over a battery-only system and a hybrid SCES/battery system controlled with the classical droop method, a comparative analysis under different scenarios is presented.

Keywords: battery lifetime; supercapacitor; decentralized control; hybrid energy storage system; droop control; MPPT algorithms

Citation: Papageorgiou, P.; Oureilidis, K.; Tsakiri, A.; Christoforidis, G. A Modified Decentralized Droop Control Method to Eliminate Battery Short-Term Operation in a Hybrid Supercapacitor/Battery Energy Storage System. *Energies* **2023**, *16*, 2858. https://doi.org/10.3390/en16062858

Academic Editor: Byoung Kuk Lee

Received: 5 March 2023
Revised: 17 March 2023
Accepted: 18 March 2023
Published: 20 March 2023

1. Introduction

Environmentally friendly renewable energy sources (RESs) such as photovoltaic units (PVs) and wind turbine generators (WTGs) are scalable and can be installed in industrial, commercial, agricultural, and residential areas [1]. Moreover, their primary sources such as solar irradiation and wind are abundant in nature. On the other hand, environmental pollution, high cost, and rapid depletion of fossil fuels are their main demerits [2]. To achieve the demanding decarbonization targets, governments worldwide are striving to replace conventional, fossil fuel-based power generation with RES-based generation [3]. Therefore, the power system's dependability on renewables has increased, raising the concerns of both the industry and academic sectors.

This changing environment has prompted the development of new microgrid architectures that provide a framework to facilitate the integration of RESs and energy storage systems [4]. A microgrid is a group of distributed energy sources, interconnected loads, and storage systems with clearly defined electrical and geographical boundaries that acts as a single entity with respect to the grid. Additionally, it has the ability to operate both in grid-connected and islanded mode [5]. The high proliferation of DC power sources along with the emergence of modern DC loads contribute to the rapid development of DC microgrids [6]. This trend is further enhanced by their inherent advantages in relation to AC, such as the absence of harmonic pollution, phase unbalances and synchronization issues, and zero reactive power flows [7]. However, their resilient operation is jeopardized by RESs volatility, abrupt load variations, unscheduled disconnections from the utility grid, and faults that may occur on the power lines [8]. These disturbances can cause DC bus voltage fluctuations and deteriorate the overall power quality. Therefore, employment of a properly controlled energy storage system to compensate for the generation-consumption mismatch is a prominent solution to improve the microgrid's stability and ensure its safe operation for end-users.

Energy-type lead–acid and lithium-ion electrochemical batteries are the most dominant energy storage types in microgrids due to their high-energy density, high efficiency, and relatively high level of maturity [9]. However, short-term (i.e., frequent) cyclic operation and high charging/discharging rates (i.e., high di/dt) significantly shrink their lifetime [10–12]. Hence, the maintenance and replacement costs are increased [13]. Additionally, their power density is limited. Thus, conventional batteries cannot handle effectively high-frequency power fluctuations. An extensive review regarding the diverse battery types can be found in [9]. On the other hand, power-type supercapacitor energy storage (SCES) systems have negligible lifetime degradation under the previous conditions and high-power density to respond instantaneously to power requirements. Nevertheless, the energy density is smaller and the capital cost is higher than those of the batteries [9]. Therefore, SCES/battery hybrid energy storage systems (HESSs) are composed of complementary storage types, exploiting their merits and concealing their demerits at the same time under a suitable control algorithm. Moreover, under the hybridization principle, the size of the battery can be significantly reduced compared to a battery-only scheme without downgrading the quality of the power system [14]. A study with particular emphasis on SCES chemistry and material design is presented in [15].

The HESSs control strategies can be mainly categorized into (i) centralized, (ii) distributed, and (iii) decentralized [16]. Their schematic diagram is illustrated in Figure 1. In centralized control, a central controller (CC) is required to adjust the local controllers (LCs) of the power and energy-type storage converters, providing strong-supervised control. The CC collects system information and transmits accordingly reference signals for the LCs through the communication infrastructure [17]. Hence, this method suffers from communication failures due to time delays during signal transfer procedures, and single points of failure. In the distributed control, there is no CC, and each LC receives local information along with data from neighboring LCs via sporadic communication links to achieve coordination between the different storage converters [18]. Thus, this method is free from single points of failure but is still prone to communication delays. Ultimately, in the decentralized strategy, the CC and the communication network are completely absent, and each LC only receives local information. Therefore, it is unaware of the status of adjacent LCs or the system status, operating independently [19].

A proper technique for power allocation among power- and energy-type storage systems is indispensable for an effective HESS. In this framework, the most widely adopted power allocation scheme for the majority of HESSs, including hybrid SCES/battery systems, is the filtration-based scheme that is implemented in [10,20–24]. This method employs a filter to decompose the net power into low- and high-frequency components to be handled by energy and power-type storage systems, respectively. However, this centralized approach is not efficient under continuous disturbances since the energy-type battery has to compensate for the low-frequency component for every single disturbance. Therefore, its service life is reduced in such cases. In [20,22], a rate limiter is inserted at the output of the filter to ensure that the battery will not react faster than its specifications allow, while in [24], the cut-off frequency of the filter is generated with fuzzy logic control (FLC) according to the energy demand, the battery cell temperature, and the SCES SoC level. In [25], the hybridization between a superconducting magnetic energy storage (SMES) system and battery is considered under a distributed approach. Specifically, the battery operates as an energy buffer for the SMES and charges or discharges at a low rate. This method, though, leads to intense battery cyclic activity if the SMES current is around its rated value. A decentralized technique for a SMES/battery HESS is introduced in [26]. It employs two droop curves with different coefficients to prioritize the power-type device over the battery when the DC bus voltage fluctuates. Nevertheless, the battery is still active even if the disturbances are small and compensable by the power-type device.

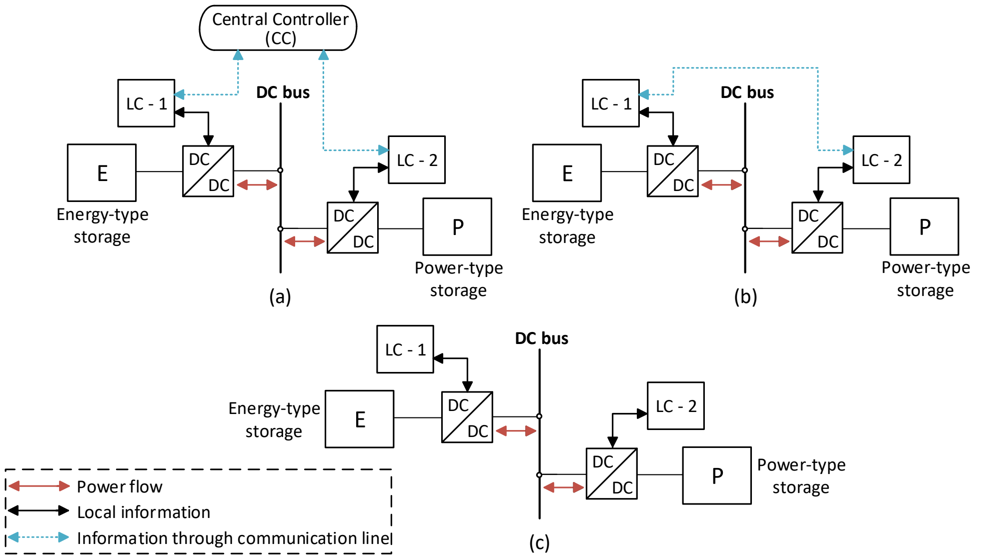

Figure 1. The schematic diagram of HESSs control methods: (**a**) Centralized; (**b**) distributed; (**c**) decentralized.

Motivated by the above considerations, this study proposes a modified droop control algorithm for a SCES/battery HESS employed in a DC microgrid. The proposed method avoids the CC and the communication links since the controllers of the SCES and battery units work independently. The SCES regulates the DC bus voltage inside a narrow band, following a droop curve. As long as the bus voltage is inside this band, the battery is kept inactive. Therefore, its short-term activity is eliminated, while the SCES is fully exploited. As soon as the bus voltage deviates from the band, the SCES is kept inactive, and the battery is triggered following a droop curve different for charging or discharging mode to stabilize the voltage. The rest of this paper is organized as follows: in Section 2, the system description and modeling are presented, and in Section 3, the control techniques are analyzed. In Section 4, the system performance is investigated under different scenarios and previously reported methods. Finally, in Section 5, conclusions are drawn highlighting the merits of the proposed control algorithm.

2. System Description and Modeling

Figure 2 depicts a schematic diagram of the examined DC microgrid. It consists of a PV system, a WTG system, a resistive load, and a HESS comprised of SCES and battery units. The HESS is employed to increase the stability of the microgrid and protect the energy-type battery from quick lifetime attenuation. All microgrid components are connected through separate DC/DC converters to a common DC bus. The resistive load is fed from a buck converter, while the PV is connected to the main DC bus through a boost converter to maximize its power output. The WTG is connected to the same bus via a three-phase uncontrolled (i.e., diode-based) rectifier followed by a boost converter to extract the maximum possible wind power, as illustrated in Figure 2. The SCES and the battery employ bidirectional half-bridge converters in a parallel active topology scheme. The mathematical modeling for the system components is provided in the upcoming sections with the necessary equations.

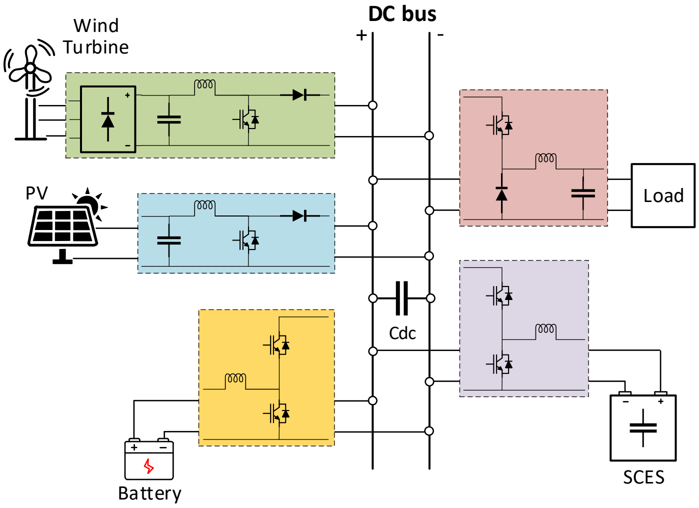

Figure 2. The schematic diagram of the overall system.

2.1. The Solar PV System

A PV panel consists of N_s solar cells in series, and Figure 3 illustrates the equivalent circuit of such a cell, while the equations that describe it are [27]:

$$i = i_{ph} - i_d - i_r \tag{1}$$

$$i_{ph} = I_{sc0}\frac{S}{S_0} + C_t\left(T - T_{ref}\right) \tag{2}$$

$$i_d = I_0(e^{\frac{qv_d}{AkT}} - 1) \tag{3}$$

$$I_0 = I_{s0}\left(\frac{T}{T_{ref}}\right)^3 e^{\frac{qE_g}{Ak}\left(\frac{1}{T_{ref}} - \frac{1}{T}\right)} \tag{4}$$

$$i_r = \frac{v_d}{R_{sh}} \tag{5}$$

$$v_d = \frac{v}{N_s} + iR_s \tag{6}$$

$$T = T_a + k_s S \tag{7}$$

where S_0 is the sun irradiation under standard test conditions (STC) in W/m^2, T_{ref} is the temperature under STC in °C, R_s is the cell series resistance in Ohm, R_{sh} is the cell shunt resistance in Ohm, I_{sc0} is the cell short circuit current at T_{ref} in A, I_{s0} is the cell diode saturation current at T_{ref} in A, E_g is the cell band energy in eV, A is cell ideality factor, C_t is the cell temperature coefficient in A/°C or °K, k_s is a coefficient that defines how solar irradiation affects cell temperature, q is the electron charge ($q = 1.6 \times 10^{-19}$ C), k is the Boltzmann constant ($k = 1.3806505 \times 10^{-23}$), S is the actual light intensity, T_a is the actual ambient temperature, v is the voltage across the entire solar panel, and i is the current flowing out of the positive terminal of the solar panel.

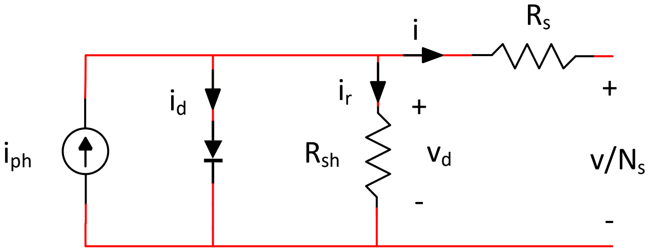

Figure 3. PV cell equivalent circuit.

The employed PV system has a rated output power of 4905 W_p and is composed of 15 SunPower SPR-E20-327 residential panels (modules) with a 327 W_p rated output power. The overall system is constructed by 3 parallel strings of 5 panels in series per string (i.e., 5S3P assembly), and its parameters are listed in Table 1.

Table 1. The PV system parameters.

Parameter	Value
Maximum Power (P_{mpp})	4905 W_p
Assembly	5S3P
Voltage at P_{max} (V_{mpp})	273.5 V
Current at P_{max} (I_{mpp})	17.94 A
Open-Circuit Voltage (V_{oc})	324.5 V
Short-Circuit Current (I_{sc})	19.38 A
Temperature Coefficient of V_{oc}	−0.272%/°C or °K
Temperature Coefficient of I_{sc}	0.04%/°C or °K
Standard Test Conditions (STC) Sun irradiation/temperature	1000 W/m^2/25 °C

2.2. The WTG System

For wind speeds between the cut-in speed (v_{cin}) and the rated speed (v_{rat}), the power generated by a wind turbine can be expressed as [27]:

$$P = 0.5 A v_{wind}^3 \rho C_p \tag{8}$$

where A is the area of the rotor blade in m^2, v_{wind} is the wind speed in m/s, ρ is the air density (1.225 kg/m^3 approximately), and C_p is the power coefficient. C_p is a function of tip speed ratio (TSR) λ and blade pitch angle β and it can be expressed as [27]:

$$C_p = c_1(c_2 - c_3\beta - c_4\beta^x - c_5)e^{-c_6} + c_7 \tag{9}$$

where $c_1 = 0.5$, $c_2 = 116 \cdot \lambda'$, $c_3 = 0.4$, $c_4 = 0$, $c_5 = 5$, $c_6 = 21 \cdot \lambda'$, $c_7 = 0.01 \cdot \lambda$ and

$$\lambda = \frac{\omega_m R_{blade}}{v_{wind}} \tag{10}$$

$$\lambda' = \frac{1}{\lambda + 0.08\beta} - \frac{0.035}{\beta^3 + 1} \tag{11}$$

where ω_m is the turbine rotational speed in rad/s and R_{blade} is the rotor blade radius in m. For wind speeds between the rated speed (v_{rat}) and the cut-out speed (v_{cout}), the wind turbine power is maintained near its rated value with pitch angle control.

The employed WTG system incorporates a small horizontal-axis wind turbine connected via a gearbox to a salient pole permanent magnet synchronous generator (PMSG) with sinusoidal back emf. The system specifications are listed in Table 2.

2.3. The SCES System

Supercapacitors (SCs), also named electric double-layer capacitors (EDLCs) or ultracapacitors, contain two conductor electrodes, a porous membrane separator, and an electrolyte in the areas between the electrodes and the separator. Due to their structure, supercapacitors have both the characteristics of conventional capacitors and electrochemical batteries. Usually, the energy is stored electrostatically in the form of static charge on the boundary surfaces between the electrolyte and the electrodes. The high-performance supercapacitors are based on nano materials to increase electrode surface area for enhanced capacitance [9]. SCs are classified into three main kinds: (i) EDLCs, (ii) pseudo-capacitors, and (iii) hybrid SCs [15]. EDLCs operate on the basis of electrostatic charge storage, pseudo-capacitors help in redox processes, and hybrid SCs store charge by polarizing electrodes and non-polarizing elements. The carbon-based EDLCs that contain carbon nanotubes (CNTs) and graphene have received considerable attention lately. Their structure has good mechanical, chemical, electrical, and thermal properties [9,15].

Table 2. The WTG system parameters.

The WT		**The PMSG**	
Parameter	**Value**	**Parameter**	**Value**
Rated power (P_{rat})	6.3 kW	Rated power (P_{rat})	6 kW
Cut-in wind speed (v_{cin})	4 m/s	Rated torque (T_{rat})	40 Nm
Rated wind speed (v_{rat})	12 m/s	Rated speed (n_{rat})	1461 rpm
Cut-out wind speed (v_{cout})	24 m/s	Stator winding resistance (R_s)	0.425 Ohm
Rotor blade diameter (D)	5.132 m	Stator d-axis inductance ($L_{s,d}$)	8.4 mH
Gearbox ratio	4	Stator q-axis inductance ($L_{s,q}$)	8.4 mH
Optimal TSR	8.18	Flux linkage (Ψ)	0.433 Wb
		No. of pole pairs (P)	5
		Moment of inertia (J)	0.01197 kgm^2
		Friction coefficient (B)	0.001189 Nms

High-power density, very short response time, and negligible lifetime degradation under frequent charging/discharging cycles or abrupt power variations are the main features of the SCES. On the other hand, it has a high capital cost, low-energy density, and high self-discharge rate [28]. The mathematical model of the SCES is given by the equations:

$$E_{SC} = \frac{1}{2} C_{SC} V_{SC}^2 \tag{12}$$

$$P_{SC} = \frac{dE_{SC}}{dt} = C_{SC} V_{SC} \frac{dV_{SC}}{dt} = V_{SC} I_{SC} \tag{13}$$

$$P_{SC,avg} = V_{SC} I_{SC,avg} \tag{14}$$

$$SOC_{sc} = \frac{E_{SC}}{E_{SC,max}} \tag{15}$$

where E_{SC} is its stored energy in J, C_{SC} is its capacitance in F, V_{SC} is its voltage in V, P_{SC} is its instantaneous power in W, I_{SC} is its instantaneous current in A, $P_{SC,avg}$ is its average power in W, $I_{SC,avg}$ is its average current in A, SOC_{SC} is its state of charge, and $E_{SC,max}$ is its maximum stored energy in J. The specifications of the small-sized SCES that is employed to eliminate the short-term cyclic activity of the battery are depicted in Table 3.

Table 3. The SCES system parameters.

Parameter	**Value**
C_{SC}	0.5 F
Rated (max) voltage ($V_{SC,max}$)	300 V
Rated (max) energy ($E_{SC,max}$)	22.5 kJ

2.4. The Battery System

The dynamic battery cell model proposed in [29] is adopted in this study. This model simulates the battery cell as a controlled voltage source in series with a fixed internal resistance, and its operation is described by the equations:

$$V_{bat} = E_0 - Ri - K\left(\frac{Q}{Q - it}\right)(it + i_{LPF}) + Ae^{-Bit} \tag{16}$$

$$V_{bat} = E_0 - Ri - K\left(\frac{Q}{it - 0.1Q}\right)i_{LPF} - K\left(\frac{Q}{Q - it}\right)it + Ae^{-Bit} \tag{17}$$

Equations (16) and (17) are valid for the discharging and the charging process of the cell, respectively. V_{bat} is its terminal voltage in V, E_0 is its constant voltage in V, K is its polarization constant in V/Ah or its polarization resistance in Ohm, Q is its maximum capacity in Ah, i is its current in A, A is its exponential zone amplitude in V, B is its exponential zone time constant inverse in $(\text{Ah})^{-1}$, R is its internal resistance in Ohm, and i_{LPF} is its filtered current in A.

The battery pack that is employed to compensate for the long-term disturbances is composed of 3000 Molicel IHR-18650B Li-ion cells with 3.6 V nominal voltage and 2.25 Ah nominal capacity. The overall system is constructed by 30 parallel strings of 100 battery cells in series per string (i.e., 100S30P assembly). Both battery cell and battery pack technical parameters are illustrated in Table 4.

Table 4. The battery cell and the battery pack parameters.

The Battery Cell		**The Battery Pack**	
Parameter	**Value**	**Parameter**	**Value**
R	0.075 Ohm	Chemistry	Li-ion
Q	2.26 Ah	Maximum power (P_{max})	21.6 kW
E_0	3.7647 V	Assembly	100S30P
A	0.4283 V	Current constraints (I_{max})	±60 A
B	3.7783 $(\text{Ah})^{-1}$	Nominal voltage (V_{nom})	360 V
K	0.01209 V/Ah	Typical capacity (Q_{typ})	67.5 Ah

3. Control Techniques

3.1. The Control Method for the PV System

The performance of a PV panel changes with the change in solar irradiation or ambient temperature according to its characteristic curves. When irradiation increases, the maximum power point (MPP) of the PV panel is increased. Therefore, both maximum PV output power P_{mpp} and voltage V_{mpp} increase, while in the case of a temperature increase, the MPP is decreased, and consequently, both P_{mpp} and V_{mpp} decrease. Hence, to extract the maximum possible solar power, it is essential to maintain the PV panel's terminal voltage at its MPP. This can be implemented through maximum power point tracking (MPPT) algorithms. In this study, the perturb and observe (P&O) algorithm [30,31] is implemented to calculate the reference PV terminal voltage. Afterwards, a PI controller is introduced to eliminate the voltage error and generate the desired duty cycle for the PV boost converter. Figure 4 shows the control technique employed for the PV system.

3.2. The Control Method for the WTG System

The performance of a WTG changes with the change in wind speed according to its characteristic curves. The power coefficient C_p can be maximum at only one value of TSR, λ_{opt}. During MPPT operation (β = 0), when wind speed increases, WTG speed must increase proportionally, as shown in Equation (10), to sustain λ at its optimal value. Hence, the extraction of the maximum possible wind power is realized. In this study, the TSR method [32,33] is employed, which requires TSR knowledge and wind and turbine speed measurements. Then, a PI controller is introduced to track the reference turbine speed and define the desired duty cycle for the WTG boost converter, as presented in Figure 4.

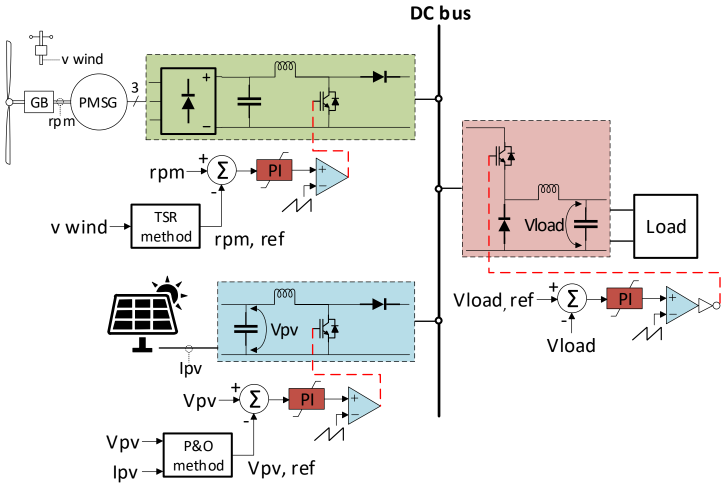

Figure 4. The control techniques for PV, WTG, and load.

3.3. The Control Method for the Load

The resistive load is connected to the main DC bus via a buck converter that regulates the voltage across the load terminals. The error between the desired and the actual load voltage is handled by a PI controller, which generates the reference duty cycle for the load converter, as depicted in Figure 4.

3.4. The Control Method for the SCES/Battery HESS

Figure 5a illustrates the working principle of the proposed control method, which is based on the DC bus voltage measurement, while Figure 5b,c depict the droop curves employed for the SCES and battery systems, respectively. As long as the DC bus voltage is inside the narrow zone defined by the V_{BUS} *zone, lower limit*, and V_{BUS} *zone, upper limit*, all the disturbances are compensated exclusively by the SCES, which charges or discharges accordingly, following its droop curve (Figure 5b). In such cases, the battery is kept inactive, as its reference current is zero (Figure 5c). Therefore, the frequent (i.e., short-term) cyclic operation of the battery is eliminated, and all the available energy capacity of the SCES is exploited.

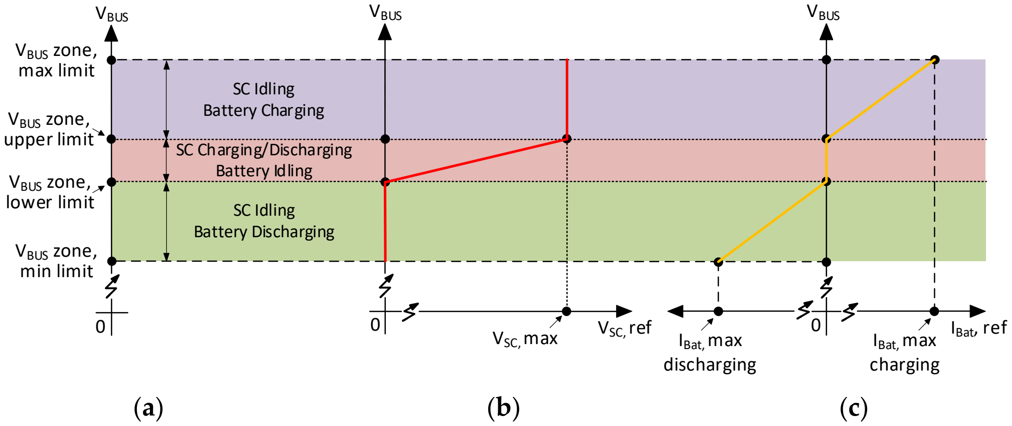

Figure 5. (**a**) The working principle of the proposed SCES/battery HESS control algorithm; (**b**) the droop curve with multiple segments for the SCES; (**c**) the droop curve with multiple segments for the battery.

As soon as the bus voltage drops below the V_{BUS} *zone, lower limit*, the SCES enters the idling state, preserving its minimum state of charge (SoC) level. Simultaneously, the battery is triggered and follows its discharging droop curve, operating in the discharging zone of Figure 5. Once the bus voltage exceeds the V_{BUS} *zone, upper limit*, the operation is derived accordingly, the SCES preserves its maximum SoC level, and the battery works in the charging zone of Figure 5. In this study, the battery discharges or charges at its maximum current, I_{Bat}, *max discharging* or I_{Bat}, *max charging*, when the minimum and maximum allowable limits for the bus voltage, V_{BUS} *zone, min limit* or V_{BUS} *zone, max limit*, are reached, respectively. These bus voltage limits are selected to establish a tolerance zone of ±10% on the DC bus, according to [34], while the inner voltage limits are selected to establish a much narrower zone of ±1.33% on the same bus.

Ultimately, the proposed control method is decentralized, since it avoids the CC and the communication links between the SCES controller and the battery controller. The complete implementation of the control algorithm is depicted in Figure 6. PI controllers are employed to track the reference current signals for the SCES and the battery, defined by the corresponding reference current generation blocks. The control parameters are listed in Table 5.

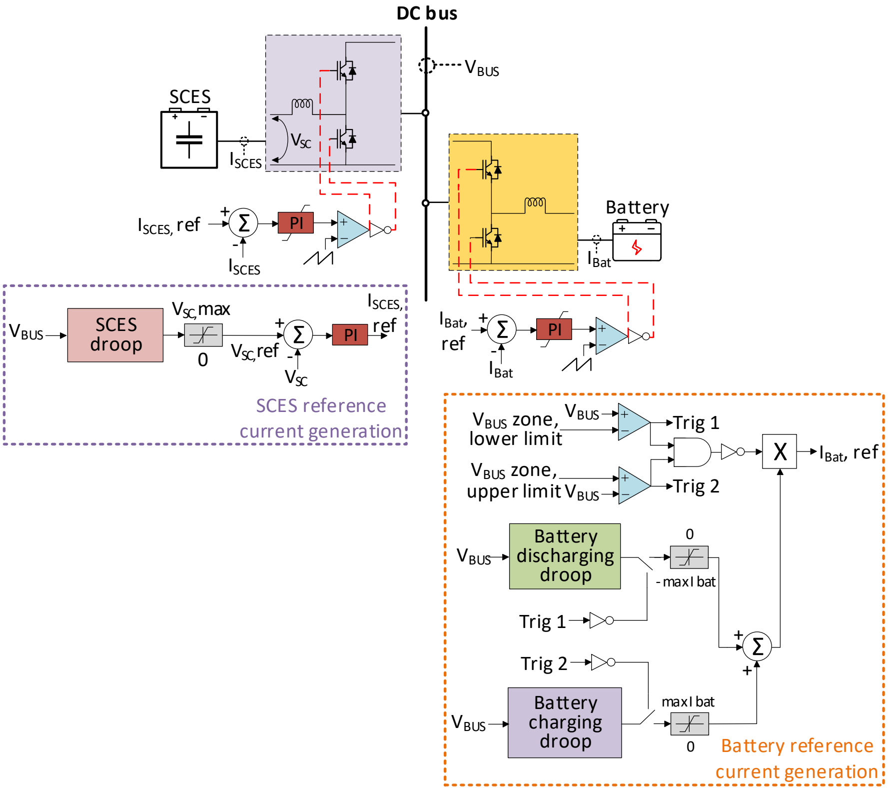

Figure 6. The complete implementation of the SCES/battery HESS control algorithm.

3.5. The Control Method for the Battery in the Battery-Only System Used for Comparison

Figure 7 illustrates the control algorithm for the battery in the battery-only system (BOS) that will be used for a comparative analysis to evaluate the effectiveness of the proposed method. It consists of two cascaded PI control loops [35]. In the outer loop, the DC bus voltage reference is compared with the actual bus voltage, and the resulting error is handled by the first PI controller, which defines the battery reference current for the inner loop. Afterwards, the error in the battery current is supervised by the second PI controller, which defines the desired duty cycle for the battery converter.

3.6. The Classical Droop Control Method for the SCES/Battery HESS Used for Comparison

The working principle of the classical decentralized droop scheme that allocates the power between a fast-responsive storage system and a battery according to the DC bus voltage variations is presented in [26]. The power sharing is realized by employing two droop curves with different slopes to charge/discharge the different storage units at different rates. Their operating modes (i.e., charging, discharging, and standby) arise according to the bus voltage measurement and the corresponding droop curves, as depicted in Figure 8, employing the SCES as the fast-responsive system. Therefore, the slope of its droop curve is lower than that of the battery. Once the references for the SCES voltage and the battery current are obtained, the low-level control for the hybrid system is implemented according to Figure 6.

Table 5. The control parameters.

Parameter	Value
Nominal bus voltage	750 V (1 p.u.)
V_{BUS} *zone, lower limit*	740 V (0.9867 p.u.)
V_{BUS} *zone, upper limit*	760 V (1.0133 p.u.)
V_{BUS} *zone, min limit*	675 V (0.9 p.u.)
V_{BUS} *zone, max limit*	825 V (1.1 p.u.)
V_{SC}*, max*	300 V
I_{Bat}*, max*	±60 A
DC bus capacitor	6 mF
Switching frequency for the SCES	10 kHz
Switching frequency for the battery	10 kHz

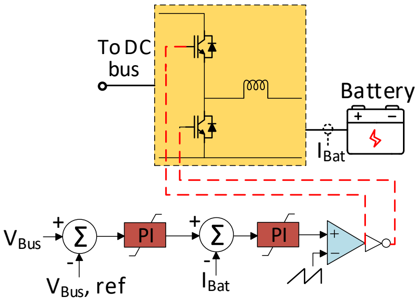

Figure 7. The control algorithm for the battery in the BOS.

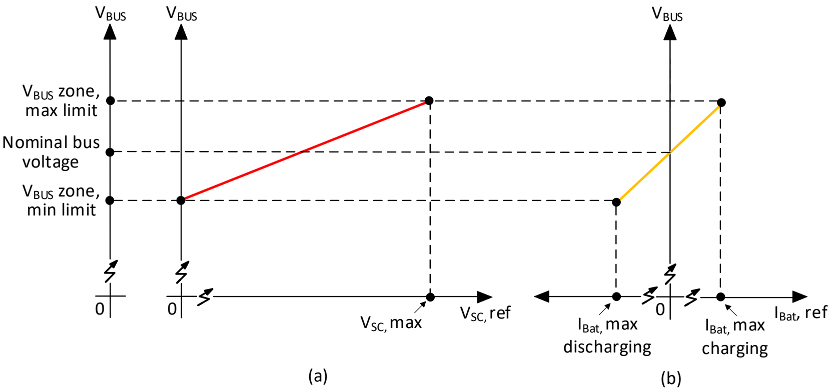

Figure 8. The classical droop control for the SCES/battery HESS: (**a**) The droop curve with low slope for the SCES; (**b**) the droop curve with high slope for the battery.

4. Simulation Results and Discussion

To evaluate the effectiveness of the proposed SCES/battery HESS, its performance is investigated under different scenarios and previously reported techniques. Initially, the proposed scheme is compared with a BOS under three different scenarios according to the SCES SoC level, namely: (i) operation with an intermediate SoC level; (ii) operation with a high SoC level; and (iii) operation with a low SoC level. Therefore, an investigation is carried out in all operating regions of the proposed algorithm, and a comparative analysis is presented for each individual scenario. Afterwards, the proposed droop technique is compared with the classical droop approach for the SCES/battery HESS. The PSIM software is utilized to conduct the simulations.

4.1. Comparison with a BOS

4.1.1. Case 1: Operation with an Intermediate SCES SoC Level

An intermediate SoC level for the SCES system is considered in this case, since its initial voltage is 200 V, along with a volatile PV generation. The duration range of the PV fluctuations is from 0.5 s up to 1 s [8]. Figure 9 indicates the power generated by the renewables and consumed by the load. The ambient temperature is fixed at 25 °C throughout the simulation, while the solar irradiation is fixed at 600 W/m^2 up to 0.5 s, 1000 W/m^2 from 0.5 s up to 1.5 s, and 400 W/m^2 from 1.5 s up to 2 s. Consequently, the PV generates 2.93 kW, 4.93 kW, and 1.93 kW, operating at its MPP, respectively. The wind speed is constant at 12 m/s, and the WT generates 5.97 kW, extracting the maximum possible wind power, while the load demand is fixed at 10 kW.

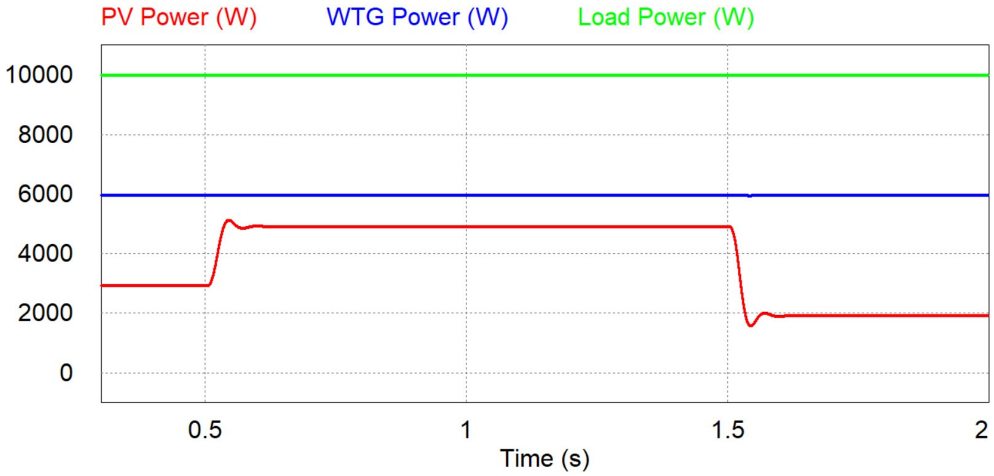

Figure 9. The power of PV, WTG, and load—Case 1.

Due to the small power deficit before 0.5 s and after 1.5 s, the bus voltage is slightly decreasing, as shown in Figure 10a. In the intervening period of time, it is slightly increasing due to the elevated PV generation (Figure 10a). However, the bus voltage is maintained inside the zone defined by the V_{BUS} *zone, lower limit* and the V_{BUS} *zone, upper limit* throughout the simulation. Therefore, all the disturbances are compensated exclusively by the droop-controlled SCES since the battery is in an idle state, as illustrated in Figure 11a,b and Figure 12a,b, respectively. The rapid-responsive SCES instantly changes from discharging to charging and vice versa at 0.5 s and at 1.5 s, respectively (Figure 11a,b). Hence, the frequent small-scale battery operation is eliminated, its rapid current variations are avoided, and its service time is improved. Additionally, the bus voltage is well maintained near its nominal value in this case, as depicted in Figure 10a.

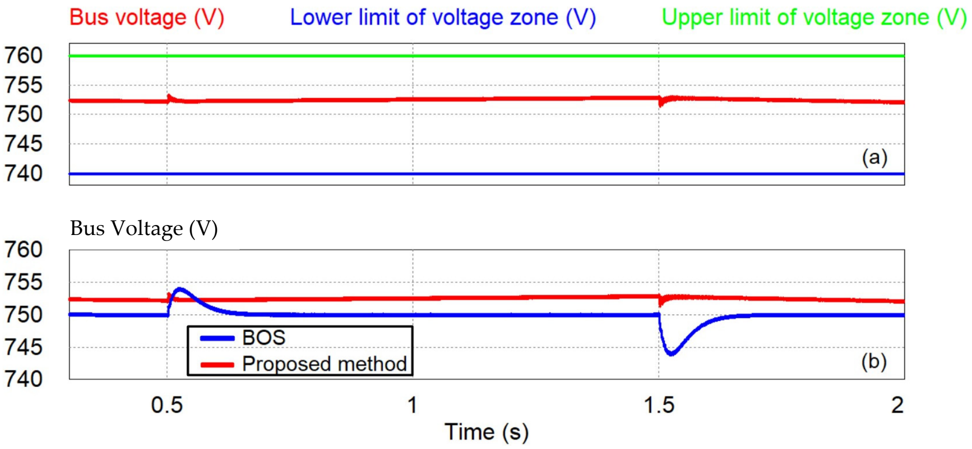

Figure 10. (**a**) The DC bus voltage and the corresponding limits in the proposed method; (**b**) the DC bus voltage in both methods—Case 1.

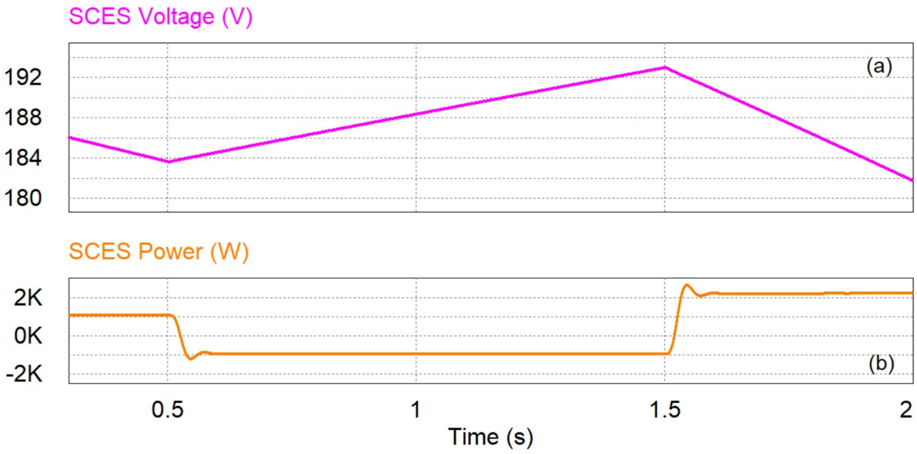

Figure 11. (**a**) The SCES voltage; (**b**) the SCES power—Case 1.

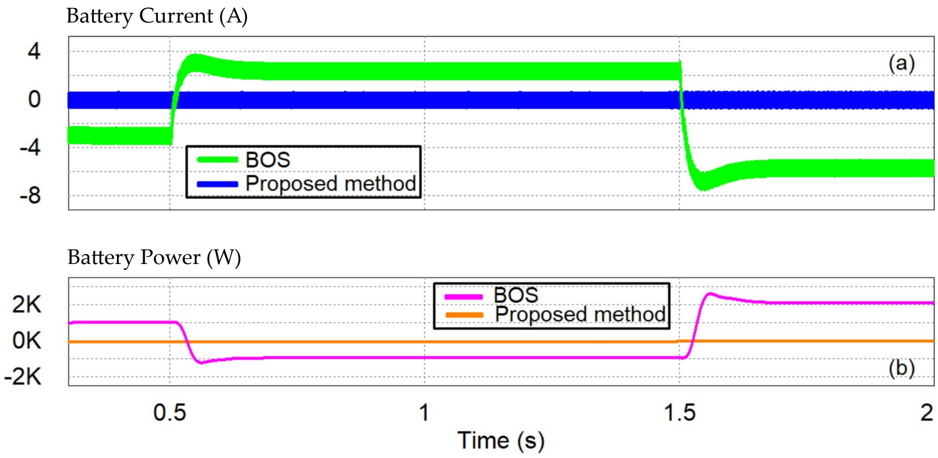

Figure 12. (**a**) The battery current; (**b**) the battery power—Case 1.

On the contrary, in the case of a BOS, an overshoot of 4 V and an undershoot of 6 V are noticed in the microgrid bus, and the stress levels for the battery are increased. It is exposed to frequent cyclic activity and abrupt current variations, as shown in Figure 12a,b. Indicatively, the battery switches from discharging to charging at 0.5 s and from charging to discharging at 1.5 s, with rates of 238 A/s and 412 A/s, respectively. These rates pose challenges for the battery manufacturer and its lifespan.

4.1.2. Case 2: Operation with a High SCES SoC Level

In this case, a high SoC level for the SCES system is considered since its initial voltage is 280 V, along with a step change in the load power at 1 s. Figure 13 indicates the power generated by the renewables and consumed by the load. Both PV and WTG operate at their MPP, generating 4.93 kW and 5.97 kW, respectively. The load demand is fixed at 8 kW up to 1 s, and then it changes sharply to 6 kW.

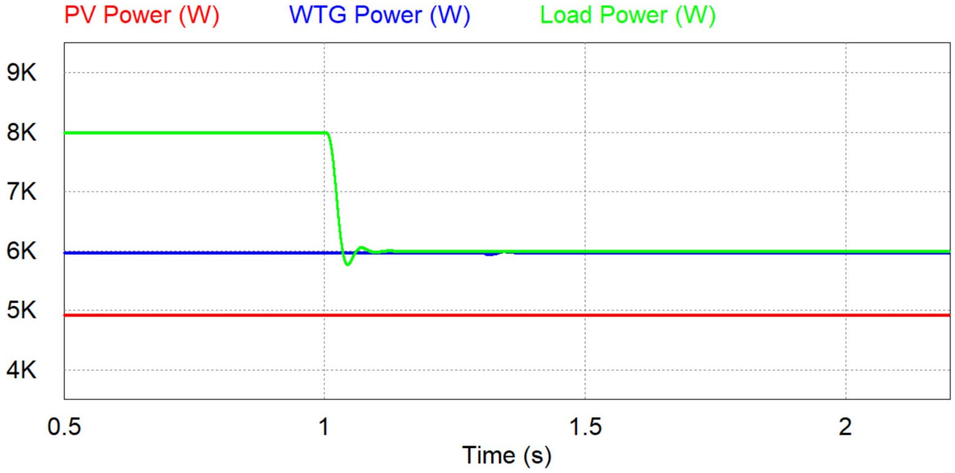

Figure 13. The power of PV, WTG, and load—Case 2.

Due to the power surplus, the bus voltage is increasing, as shown in Figure 14a. Right after the load step reduction, the rise rate for the voltage gets bigger than before, since the power surplus is increased. Consequently, the bus voltage exceeds the V_{BUS} *zone, upper limit* at 1.27 s as shown in Figure 14a. This time instant, the SCES reaches its maximum voltage, compensating the power surplus prior to this time instant, as depicted in Figure 15a,b, respectively. Therefore, until then, the battery is inactive (Figure 16a,b) and operating according to the proposed control method. Afterwards, the SCES enters the idle state, and the battery is triggered to charge, following its charging droop curve. Finally, the bus voltage is stabilized at 774 V, while the battery is charging at 12.9 A, as illustrated in Figures 14a and 16a, respectively.

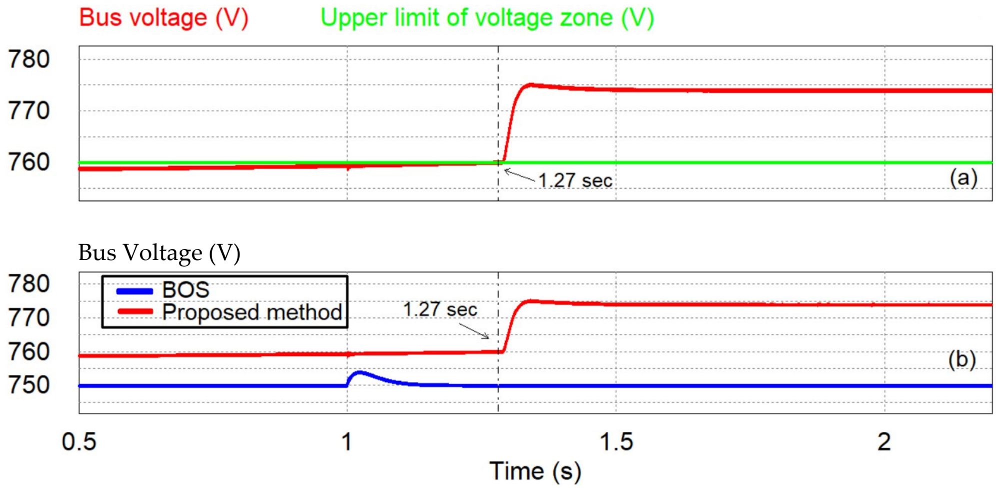

Figure 14. (**a**) The DC bus voltage and the upper voltage limit in the proposed method; (**b**) the DC bus voltage in both methods—Case 2.

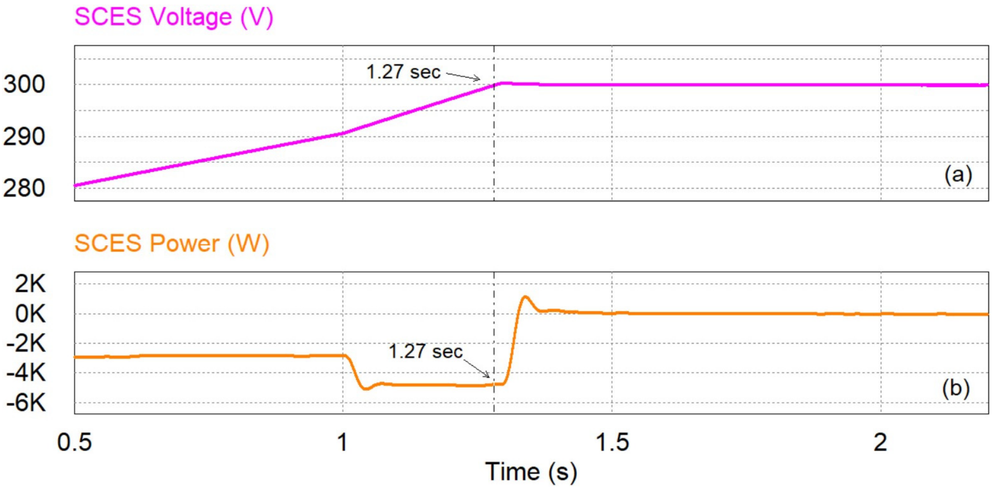

Figure 15. (**a**) The SCES voltage; (**b**) the SCES power—Case 2.

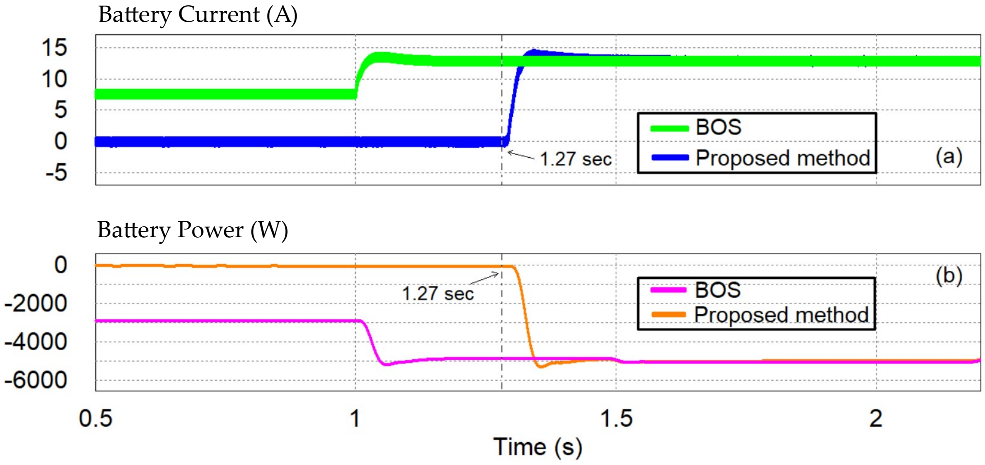

Figure 16. (**a**) The battery current; (**b**) the battery power—Case 2.

On the other hand, in the case of a BOS, the battery compensates the surplus before and after the load step reduction, charging with currents of 7.7 A and 12.9 A, respectively (Figure 16a). Thus, it regulates the bus voltage at its nominal value (Figure 14b). Once the load is reduced, the battery current changes with a rate of 288 A/s. However, under the proposed method, the battery is kept idle up to 1.27 s, and then the SCES is withdrawn while the battery is triggered to charge at a rate of 479 A/s.

4.1.3. Case 3: Operation with a Low SCES SoC Level

In this case, a low SoC level for the SCES system is considered since its initial voltage is 40 V, along with a step change in the load power at 1.5 s. Figure 17 depicts the power generated by the renewables and consumed by the load. Both PV and WTG follow the reference signals defined by their MPPT algorithms, generating 4.93 kW and 4.61 kW, respectively. The load demand is fixed at 10 kW up to 1.5 s, and then it changes abruptly to 13 kW.

Due to the power deficit, the bus voltage is decreasing, as shown in Figure 18a. Consequently, it becomes smaller than the V_{BUS} *zone*, *lower limit* at 1.25 s (Figure 18a). This time instant, the energy capacity of the SCES is depleted since it follows its droop curve and compensates the power deficit prior to this time instant, as depicted in Figure 19. Therefore, until then, the proposed control method keeps the battery idle (Figure 20a,b). Afterwards, the SCES enters the idle state, and the battery is triggered to discharge, following its discharging droop curve. The bus voltage is stabilized at 738.7 V, while the battery is discharging at 1.2 A, as illustrated in Figures 18a and 20a, respectively. Finally, at 1.5 s, the load demand is increased, and therefore, the battery stabilizes the bus voltage at 729.9 V discharging at 9.3 A, according to its corresponding droop curve, as indicated in Figures 18a and 20a, respectively.

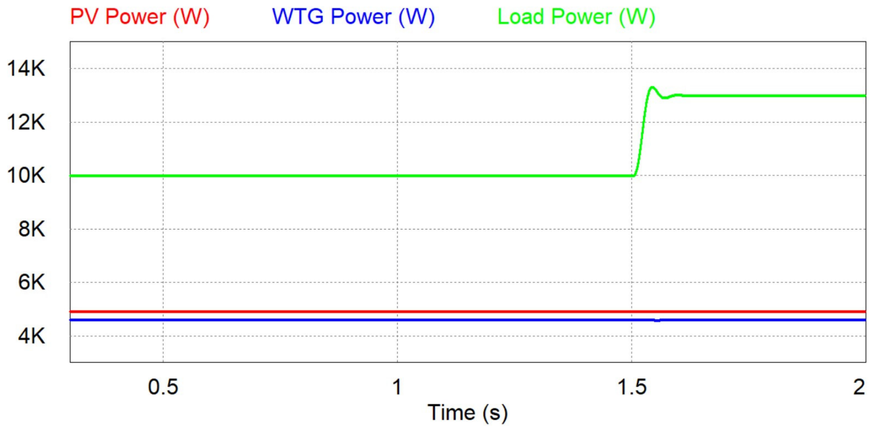

Figure 17. The power of PV, WTG, and load—Case 3.

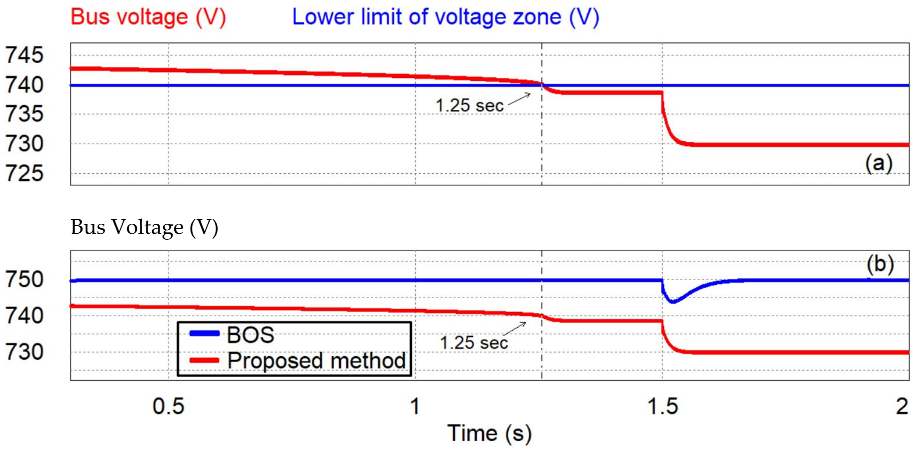

Figure 18. (**a**) The DC bus voltage and the lower voltage limit in the proposed method; (**b**) the DC bus voltage in both methods—Case 3.

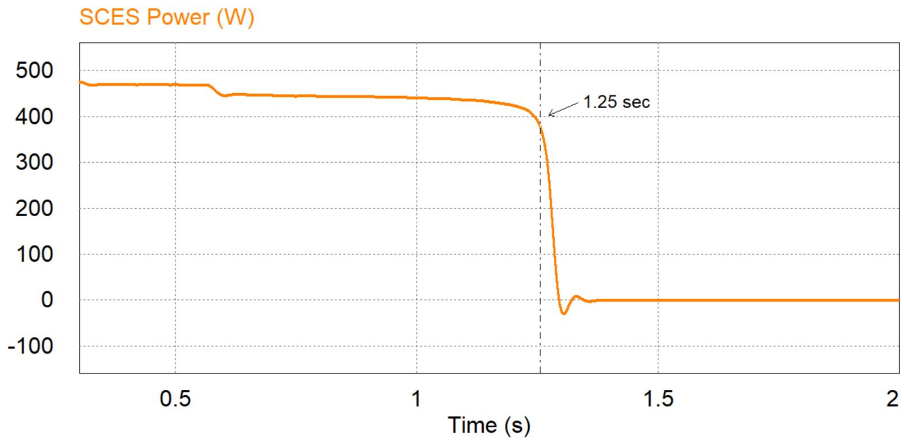

Figure 19. The SCES power—Case 3.

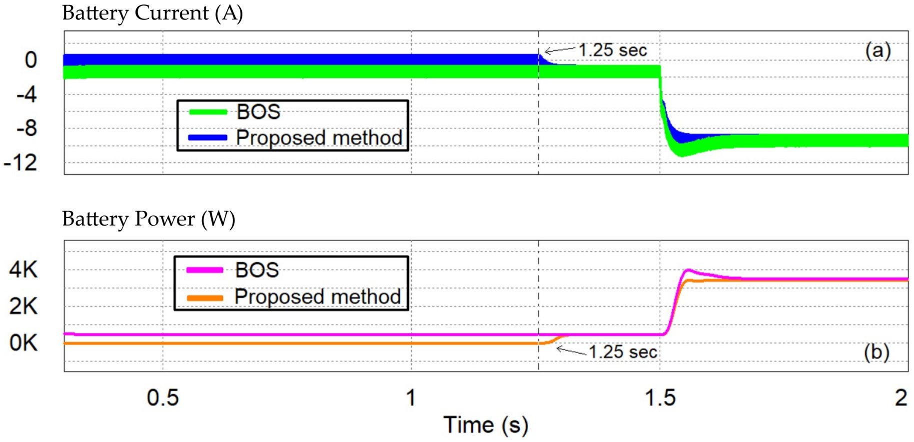

Figure 20. (**a**) The battery current; (**b**) the battery power—Case 3.

On the contrary, in the case of a BOS, the battery compensates the deficit before and after the load increase, discharging with currents of 1.2 A and 9.3 A, respectively (Figure 20a). Thus, it regulates the bus voltage at its nominal value (Figure 18b). However, once the load is increased, the battery current changes with a rate of 436 A/s. Under the proposed method, though, the corresponding battery rate for the same load change is 413 A/s. Therefore, the droop control can reduce the working rates for the battery compared to a BOS when it compensates disturbances outside of the zone in which the SCES is active and the battery is inactive.

4.1.4. Comparison among the Previous Cases

Table 6 presents a comprehensive comparison among the previous three assessments in the presence of a BOS and a SCES/battery HESS controlled with the proposed method. The comparison includes the maximum DC bus voltage deviation from its nominal value, the battery status, and the battery current variations. From this table, it can be concluded that the SCES eliminates the frequent cyclic activity for the battery and reduces its current variations when the bus voltage is outside the narrow zone. Therefore, the presented scheme prolongs the battery's lifespan.

Table 6. Comparison among the previous assessments in the presence of a BOS and a SCES/battery HESS controlled with the proposed scheme.

Case	Parameter	BOS	SCES/Battery HESS
1	Maximum DC bus voltage deviation	6.19 V	3.39 V
	Battery status	t ≤ 0.5 s, discharging 0.5 s < t ≤ 1.5 s, charging t > 1.5 s, discharging	Idling
	Battery current variations	238 A/s @ 0.5 s 412 A/s @ 1.5 s	0
2	Maximum DC bus voltage deviation	4 V	25.29 V
	Battery status	Charging	t ≤ 1.27 s, idling t > 1.27 s, charging
	Battery current variations	288 A/s @ 1 s	479 A/s @ 1.27 s
3	Maximum DC bus voltage deviation	6.2 V	20.2 V
	Battery status	Discharging	t ≤ 1.25 s, idling t > 1.25 s, discharging
	Battery current variations	436 A/s @ 1.5 s	43.3 A/s @ 1.25 s 413 A/s @ 1.5 s

4.2. Comparison with the Classical Droop Technique

Here, the modified droop control method is compared with the classical droop approach for the SCES/battery HESS, considering a fluctuating PV generation profile [8]. The SoC level for the SCES system is set to 50% in both cases. Figure 21 indicates the power generated by the PV. The ambient temperature is fixed at 25 °C throughout the simulation, while the solar irradiation varies in the range of 400 W/m^2 up to 1100 W/m^2. Consequently, the PV generation fluctuates from 1.93 kW up to 5.43 kW, operating at its MPP. The wind speed is constant at 12 m/s and the WT generates 5.97 kW, extracting the maximum possible wind power, while the load demand is fixed at 10 kW.

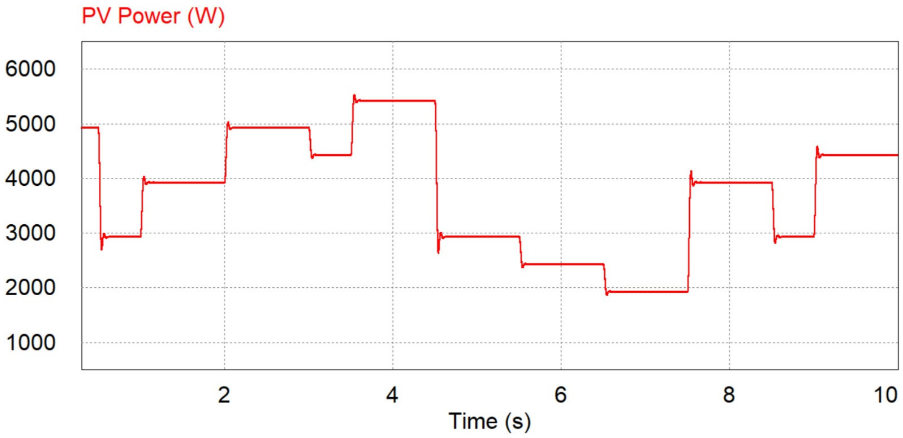

Figure 21. The power of PV.

As shown in Figure 22a, the bus voltage is maintained inside the zone defined by the V_{BUS} *zone, lower limit* and the V_{BUS} *zone, upper limit* throughout the simulation when the proposed control method is employed. Therefore, all the disturbances are compensated exclusively by the rapid-responsive SCES, since the battery is in an idle state, as illustrated in Figure 23a,b and Figure 24a,b, respectively. Hence, the frequent small-scale cyclic operation for the battery is eliminated, and its service time is prolonged. Additionally, the bus voltage is satisfactorily maintained near its nominal value, as depicted in Figure 22a.

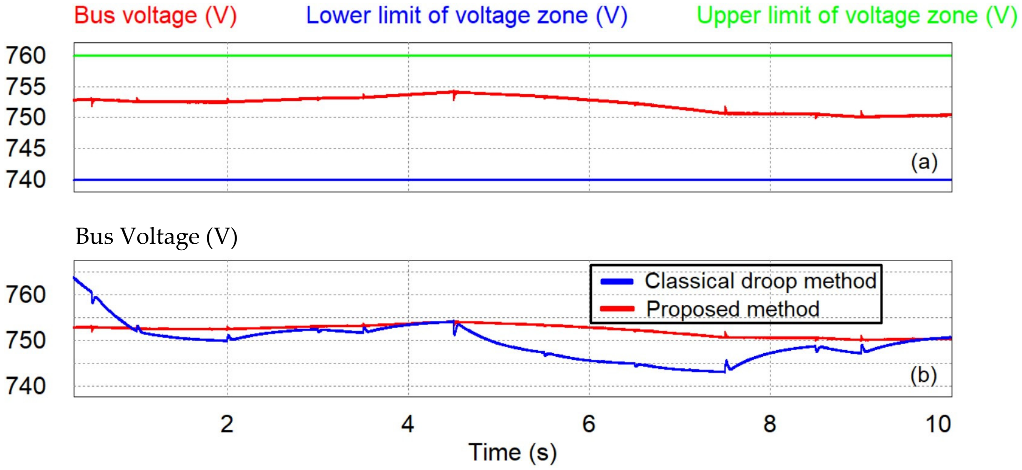

Figure 22. (**a**) The DC bus voltage and the corresponding limits in the proposed method; (**b**) the DC bus voltage in both methods.

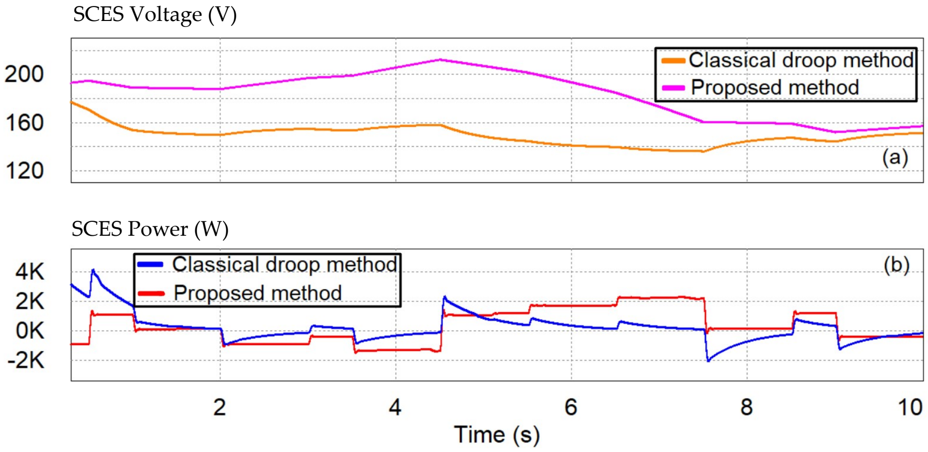

Figure 23. (**a**) The SCES voltage in both methods; (**b**) the SCES power in both methods.

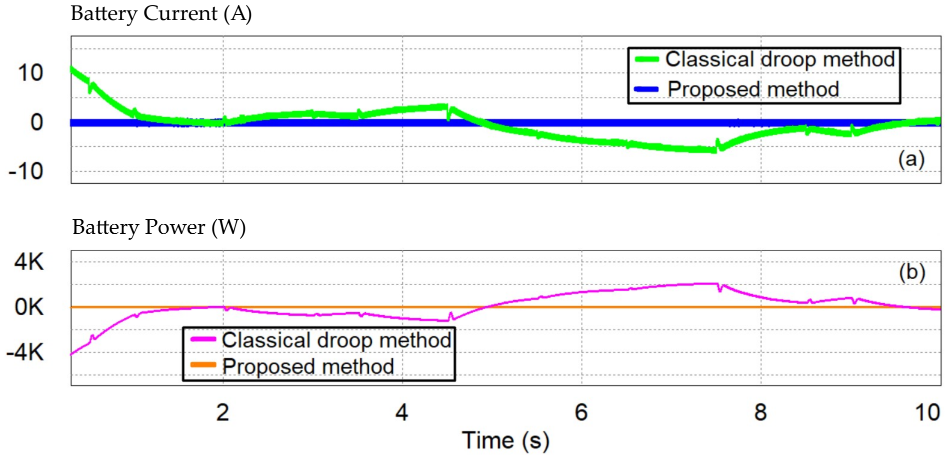

Figure 24. (**a**) The battery current; (**b**) the battery power.

On the contrary, when the classical droop method is employed, the fluctuation of the bus voltage around its nominal value is noticeably higher than that of the proposed scheme (Figure 22b). Indicatively, the bus voltage is equal to 743 V at 7.5 s. Both the SCES and the battery respond according to the bus voltage variations following their droop curves. Therefore, when the bus voltage decreases (increases), the SCES voltage decreases (increases) (Figures 22b and 23a), and as long as the bus voltage is greater (lower) than its nominal value, the battery charges (discharges) (Figures 22b and 24a). Consequently, the classical droop method is unable to eliminate the short-term activity of the battery but ensures smooth current variations for it. Table 7 presents a comprehensive comparison between the proposed droop method and the classical droop technique.

Table 7. Comparison among the proposed droop method and the classical droop approach for the SCES/battery HESS.

Parameter	Classical Droop Method	Proposed Droop Method
Maximum DC bus voltage deviation	14 V	4.47 V
Battery status	$t \leq 4.93$ s, charging 4.93 s $< t \leq 9.63$ s, discharging $t > 9.63$ s, charging	Idling
Maximum battery current variation	14.7 A/s @ 0.5 s	0

5. Conclusions

A modified droop control algorithm for a SCES/battery HESS that is employed in a DC microgrid is proposed in this study. Unlike the centralized and distributed control methods, the presented scheme avoids the CC and communication links since the controllers of SCES and battery systems work independently. To eliminate the frequent cyclic activity and improve the lifetime of the energy-type battery, the power-type SCES is employed to regulate the bus voltage inside a narrow zone following its droop curve. Inside this zone, the battery is kept in idle mode. As soon as the bus voltage deviates from this band, the SCES is kept inactive, and the battery is triggered following a droop curve different for charging or discharging mode to stabilize the bus voltage. To evaluate the effectiveness of the proposed method under different scenarios and previously reported techniques, a comparison is made with a BOS and a hybrid SCES/battery system controlled with the classical droop method, and the results are summarized in Tables. The presented control scheme eliminates the short-term cyclic operation of the battery. Additionally, compared to a BOS, it reduces the battery working rates in cases where the bus voltage is outside the narrow band, to further improve its service time, and compared to the classical droop scheme, it regulates the bus voltage more effectively. Indicatively, the proposed droop method, in the first case of comparison with a BOS, zeroes the short-term activity of the battery and reduces the maximum bus voltage deviation by 45.23%, while in the third case of comparison with a BOS, it reduces the battery current variation by 5.28% for the same load step change. Furthermore, when it is compared with the classical droop method, it zeroes the short-term activity of the battery and reduces the maximum bus voltage deviation by 68.07%. On the other hand, once the SCES is withdrawn, the battery is triggered with a high charging or discharging rate.

Author Contributions: Conceptualization, P.P., K.O. and G.C.; methodology, P.P. and K.O.; software, P.P. and A.T.; validation, P.P., K.O. and A.T.; formal analysis, P.P. and A.T.; investigation, P.P.; resources, P.P. and A.T.; writing—original draft preparation, P.P. and K.O.; writing—review and editing, P.P., K.O. and G.C.; visualization, P.P.; supervision, K.O. and G.C.; project administration, G.C.; funding acquisition, G.C. All authors have read and agreed to the published version of the manuscript.

Funding: We acknowledge support of this work by the project "Development of New Innovative Low-Carbon Energy Technologies to Enhance excellence in the Region of Western Macedonia" (MIS 5047197) under the Action "Reinforcement of the Research and Innovation Infrastructure", funded by the Operational Programme "Competitiveness, Entrepreneurship and Innovation" (NSRF 2014–2020) and co-financed by Greece and the European Union (European Regional Development Fund).

Data Availability Statement: No new data were created or analyzed in this study. Data sharing is not applicable to this article.

Conflicts of Interest: The authors declare no conflict of interest. The funders had no role in the design of the study; in the collection, analyses, or interpretation of data; in the writing of the manuscript; or in the decision to publish the results.

References

1. Tan, K.M.; Babu, T.S.; Ramachandaramurthy, V.K.; Kasinathan, P.; Solanki, S.G.; Raveendran, S.K. Empowering smart grid: A comprehensive review of energy storage technology and application with renewable energy integration. *J. Energy Storage* **2021**, *39*, 102591. [CrossRef]
2. Sebestyén, V. Renewable and Sustainable Energy Reviews: Environmental impact networks of renewable energy power plants. *Renew. Sustain. Energy Rev.* **2021**, *151*, 111626. [CrossRef]
3. A European Green Deal. Available online: https://ec.europa.eu/info/strategy/priorities-2019-2024/european-green-deal_en (accessed on 11 January 2023).
4. Oureilidis, K.; Malamaki, K.-N.; Gallos, K.; Tsitsimelis, A.; Dikaiakos, C.; Gkavanoudis, S.; Cvetkovic, M.; Mauricio, J.M.; Ortega, J.M.M.; Ramos, J.L.; et al. Ancillary Services Market Design in Distribution Networks: Review and Identification of Barriers. *Energies* **2020**, *13*, 917. [CrossRef]
5. Yang, N.; Paire, D.; Gao, F.; Miraoui, A. Power Management Strategies for Microgrid—A Short Review. In Proceedings of the 2013 IEEE Industry Applications Society Annual Meeting, Lake Buena Vista, FL, USA, 6–11 October 2013.

6. Sun, J.; Lin, W.; Hong, M.; Loparo, K.A. Voltage Regulation of DC-Microgrid with PV and Battery. *IEEE Trans. Smart Grid* **2020**, *11*, 4662–4675. [CrossRef]
7. Dragicevic, T.; Lu, X.; Vasquez, J.C.; Guerrero, J.M. DC Microgrids—Part II: A Review of Power Architectures, Applications, and Standardization Issues. *IEEE Trans. Power Electron.* **2016**, *31*, 3528–3549. [CrossRef]
8. Ni, F.; Zheng, Z.; Xie, Q.; Xiao, X.; Zong, Y.; Huang, C. Enhancing resilience of DC microgrids with model predictive control based hybrid energy storage system. *Int. J. Electr. Power Energy Syst.* **2021**, *128*, 106738. [CrossRef]
9. Luo, X.; Wang, J.; Dooner, M.; Clarke, J. Overview of current development in electrical energy storage technologies and the application potential in power system operation. *Appl. Energy* **2015**, *137*, 511–536. [CrossRef]
10. Li, J.; Gee, A.M.; Zhang, M.; Yuan, W. Analysis of battery lifetime extension in a SMES-battery hybrid energy storage system using a novel battery lifetime model. *Energy* **2015**, *86*, 175–185. [CrossRef]
11. Zhang, Q.; White, R.E. Capacity fade analysis of a lithium ion cell. *J. Power Sour.* **2008**, *179*, 793–798. [CrossRef]
12. Ruan, H.; Barreras, J.V.; Engstrom, T.; Merla, Y.; Millar, R.; Wu, B. Lithium-ion battery lifetime extension: A review of derating methods. *J. Power Sour.* **2023**, *563*, 232805. [CrossRef]
13. Ndiaye, A.; Locment, F.; De Bernardinis, A.; Sechilariu, M.; Redondo-Iglesias, E. A Techno-Economic Analysis of Energy Storage Components of Microgrids for Improving Energy Management Strategies. *Energies* **2022**, *15*, 1556. [CrossRef]
14. Lee, N.; Nee, C.H.; Yap, S.S.; Tham, K.K.; You, A.H.; Yap, S.L.; Arof, A.K.B.M. Capacity Sizing of Embedded Control Battery–Supercapacitor Hybrid Energy Storage System. *Energies* **2022**, *15*, 3783. [CrossRef]
15. Yaseen, M.; Khattak, M.A.K.; Humayun, M.; Usman, M.; Shah, S.S.; Bibi, S.; Hasnain, B.S.U.; Ahmad, S.M.; Khan, A.; Shah, N.; et al. A Review of Supercapacitors: Materials Design, Modification, and Applications. *Energies* **2021**, *14*, 7779. [CrossRef]
16. Olivares, D.E.; Mehrizi-Sani, A.; Etemadi, A.H.; Canizares, C.A.; Iravani, R.; Kazerani, M.; Hajimiragha, A.H.; Gomis-Bellmunt, O.; Saeedifard, M.; Palma-Behnke, R.; et al. Trends in Microgrid Control. *IEEE Trans. Smart Grid* **2014**, *5*, 1905–1919. [CrossRef]
17. Lin, X.; Zamora, R. Controls of hybrid energy storage systems in microgrids: Critical review, case study and future trends. *J. Energy Storage* **2022**, *47*, 103884. [CrossRef]
18. Han, Y.; Zhang, K.; Li, H.; Coelho, E.A.; Guerrero, J.M. MAS-Based Distributed Coordinated Control and Optimization in Microgrid and Microgrid Clusters: A Comprehensive Overview. *IEEE Trans. Power Electron.* **2018**, *33*, 6488–6508. [CrossRef]
19. Abhishek, A.; Ranjan, A.; Devassy, S.; Verma, B.K.; Ram, S.K.; Dhakar, A.K. Review of hierarchical control strategies for DC microgrid. *IET Renew. Power Gener.* **2020**, *14*, 1631–1640. [CrossRef]
20. Kollimalla, S.K.; Mishra, M.K.; Ukil, A.; Gooi, H.B. DC Grid Voltage Regulation Using New HESS Control Strategy. *IEEE Trans. Sustain. Energy* **2017**, *8*, 772–781. [CrossRef]
21. Sarojini, R.K.; Palanisamy, K.; Sanjeevikumar, P.; Nielsen, J.B.H. Inertia emulation control technique based frequency control of grid-connected single-phase rooftop photovoltaic system with battery and supercapacitor. *IET Renew. Power Gener.* **2020**, *14*, 1156–1163. [CrossRef]
22. Jithin, S.; Rajeev, T. Novel adaptive power management strategy for hybrid AC/DC microgrids with hybrid energy storage systems. *J. Power Electron.* **2022**, *22*, 2056–2068. [CrossRef]
23. Siad, S.B.; Iovine, A.; Damm, G.; Galai-Dol, L.; Netto, M. Nonlinear Hierarchical Easy-to-Implement Control for DC MicroGrids. *Energies* **2022**, *15*, 969. [CrossRef]
24. Sidharthan, V.P.; Kashyap, Y.; Kosmopoulos, P. Adaptive-Energy-Sharing-Based Energy Management Strategy of Hybrid Sources in Electric Vehicles. *Energies* **2023**, *16*, 1214. [CrossRef]
25. Li, J.; Xiong, R.; Mu, H.; Cornélusse, B.; Vanderbemden, P.; Ernst, D.; Yuan, W. Design and real-time test of a hybrid energy storage system in the microgrid with the benefit of improving the battery lifetime. *Appl. Energy* **2018**, *218*, 470–478. [CrossRef]
26. Li, J.; Yang, Q.; Robinson, F.; Liang, F.; Zhang, M.; Yuan, W. Design and test of a new droop control algorithm for a SMES/battery hybrid energy storage system. *Energy* **2017**, *118*, 1110–1122. [CrossRef]
27. POWERSIM User Manual. Available online: https://www.powersimtech.com/wp-content/uploads/2021/01/PSIMUser-Manual.pdf (accessed on 11 January 2023).
28. Díaz-González, F.; Sumper, A.; Gomis-Bellmunt, O.; Villafáfila-Robles, R. A review of energy storage technologies for wind power applications. *Renew. Sustain. Energy Rev.* **2012**, *16*, 2154–2171. [CrossRef]
29. Tremblay, O.; Dessaint, L.-A. Experimental Validation of a Battery Dynamic Model for EV Applications. *World Electr. Veh. J.* **2009**, *3*, 289–298. [CrossRef]
30. de Brito, M.A.G.; Galotto, L.; Sampaio, L.P.; e Melo, G.d.A.; Canesin, C.A. Evaluation of the Main MPPT Techniques for Photovoltaic Applications. *IEEE Trans. Ind. Electron.* **2013**, *60*, 1156–1167. [CrossRef]
31. Sera, D.; Mathe, L.; Kerekes, T.; Spataru, S.V.; Teodorescu, R. On the Perturb-and-Observe and Incremental Conductance MPPT Methods for PV Systems. *IEEE J. Photovolt.* **2013**, *3*, 1070–1078. [CrossRef]
32. Kotb, K.M.; Elmorshedy, M.F.; Salama, H.S.; Dán, A. Enriching the stability of solar/wind DC microgrids using battery and superconducting magnetic energy storage based fuzzy logic control. *J. Energy Storage* **2022**, *45*, 103751. [CrossRef]
33. Abdullah, M.A.; Yatim, A.H.M.; Tan, C.W.; Saidur, R. A review of maximum power point tracking algorithms for wind energy systems. *Renew. Sustain. Energy Rev.* **2012**, *16*, 3220–3227. [CrossRef]

34. IEEE Recommended Practice for the Design and Application of Power Electronics in Electrical Power Systems. In *IEEE Std 1662–2016 (Revision of IEEE Std 1662–2008)*; IEEE: Piscataway, NJ, USA, 2017; pp. 1–68.
35. Salama, H.S.; Kotb, K.M.; Vokony, I.; Dán, A. The Role of Hybrid Battery–SMES Energy Storage in Enriching the Permanence of PV–Wind DC Microgrids: A Case Study. *Eng* **2022**, *3*, 207–223. [CrossRef]